Check for updates

Activating a high-spin iron(II) complex to thermal spin-crossover with an inert non-isomorphous molecular dopant†

Malcolm A. Halcrow, [ID] *[a] Hari Babu Vasili,[b] Christopher M. Pask,[a] Alexander N. Kulak[a] and Oscar Cespedes[b]

[Fe(bpp)$_2$][ClO$_4$]$_2$ (bpp = 2,6-bis{pyrazol-1-yl}pyridine; monoclinic, $C2/c$) is high-spin between 5–300 K, and crystallises with a highly distorted molecular geometry that lies along the octahedral–trigonal prismatic distortion pathway. In contrast, [Ni(bpp)$_2$][ClO$_4$]$_2$ (monoclinic, $P2_1$) adopts a more regular, near-octahedral coordination geometry. Gas phase DFT minimisations (ω-B97X-D/6-311G**) of [M(bpp)$_2$]$^{2+}$ complexes show the energy penalty associated with that coordination geometry distortion runs as M^{2+} = Fe^{2+} (HS) ≈ Mn^{2+} (HS) < Zn^{2+} ≈ Co^{2+} (HS) ≲ Cu^{2+} ≪ Ni^{2+} ≪ Ru^{2+} (LS; HS = high-spin, LS = low-spin). Slowly crystallised solid solutions [Fe$_x$Ni$_{1-x}$(bpp)$_2$][ClO$_4$]$_2$ with x = 0.53 (**1a**) and 0.74 (**2a**) adopt the $P2_1$ lattice, while x = 0.87 (**3a**) and 0.94 (**4a**) are mixed-phase materials with the high-spin $C2/c$ phase as the major component. These materials exhibit thermal spin-transitions at $T_{\frac{1}{2}}$ = 250 ± 1 K which occurs gradually in **1a**, and abruptly and with narrow thermal hysteresis in **2a–4a**. The transition proceeds to 100% completeness in **1a** and **2a**; that is, the 26% Ni doping in **2a** is enough to convert high-spin [Fe(bpp)$_2$][ClO$_4$]$_2$ into a cooperative, fully SCO-active material. These results were confirmed crystallographically for **1a** and **2a**, which revealed similarities and differences between these materials and the previously published [Fe$_x$Ni$_{1-x}$(bpp)$_2$][BF$_4$]$_2$ series. Rapidly precipitated powders with the same compositions (**1b–4b**) mostly resemble **1a–4a**, except that **2b** is a mixed-phase material; **2b–4b** also contain a fraction of amorphous solid in addition to the two crystal phases. The largest iron fraction that can be accommodated by the $P2_1$ phase in this system is 0.7 ± 0.1.

Introduction

Metal–organic spin-crossover (SCO) compounds[1–3] continue to be widely investigated as switching components in functional materials,[4–7] and for a variety of prototype nanoscale and macroscopic device applications.[8–12] Such compounds also have a more fundamental interest, as mechanistic probes of phase transitions and other transformations in the crystalline phase.[13,14] Iron(II) complexes of 2,6-di(pyrazol-1-yl)pyridine derivatives are some the most studied materials for SCO

research.[15–17] Their popularity reflects the synthetic versatility of the bpp ligand family, which allows substituents to be appended to any position of the ligand framework. Appropriately positioned substituents can exert a steric or electronic influence on the metal spin state, giving some predictable control over its SCO temperature.[18,19] Alternatively, [Fe(bpp)$_2$]$^{2+}$ switching centres bearing functional or tether group substituents have yielded a variety of multifunctional molecules, materials and nanostructures.[20–25]

However, a disadvantage of [Fe(bpp)$_2$]$^{2+}$ derivatives for SCO applications is that the high-spin complexes are prone to an angular Jahn–Teller distortion in the solid state.[26] This is an evolution of their coordination geometry along the O_h–D_{3h} coordinate, constrained by the geometry of the tridentate bpp ligand.[16] The distortion is energetically facile, and a range of distorted geometries are computationally accessible to [Fe(bpp)$_2$]$^{2+}$ derivatives around room temperature.[26–28] Hence, the observation of distorted *vs.* undistorted geometries in a particular crystalline compound is dictated by packing considerations.[29] Materials containing distorted molecules are often inactive towards SCO, since conversion of distorted high-spin

*[a] School of Chemistry, University of Leeds, Woodhouse Lane, Leeds, LS2 9JT, UK.
E-mail: m.a.halcrow@leeds.ac.uk*
[b] School of Physics and Astronomy, University of Leeds, W. H. Bragg Building, Leeds, LS2 9JT, UK

to undistorted low-spin molecular structures is kinetically inhibited by the solid lattice.[27]

Salts of the prototype complex $[Fe(bpp)_2]^{2+}$ are a good example of this. The high-spin form of $[Fe(bpp)_2][BF_4]_2$ has a regular coordination geometry, that deviates only slightly from idealised D_{2d} symmetry (Fig. 1).[26] That allows it to undergo an abrupt thermal spin-transition just below room temperature, making it a useful testbed for new materials applications[30–32] and computational method development.[33,34] In contrast the ClO_4^-, PF_6^-, SbF_6^-, $CF_3SO_3^-$ and I^-/I_3^- salts of that complex all adopt highly distorted coordination geometries, and remain high-spin on cooling (Fig. 1).[26,28,35–37]

Solid solutions of SCO materials with isomorphous, inert dopants are an established tool for elucidating the lattice energetics of SCO processes.[38–55] We, and others, have also investigated doping as a way to introduce new functionality into SCO materials.[42,55–60] Two examples are particularly relevant to this work, where doping a complex into a host lattice changes its spin state properties. First, low-spin $[Fe(terpy)_2][ClO_4]_2$ (terpy = 2,2':6',2″-terpyridine) is activated towards light-induced spin state trapping[38] at low temperatures when doped into isomorphous $[Mn(terpy)_2][ClO_4]_2$.[56] Second, two families of solid solutions of different, non-isomorphous SCO complexes exhibit simultaneous, allosteric switching of both their component molecules.[57–59] These examples highlight that SCO properties can be manipulated, by changes to the localised chemical pressure exerted on switchable molecules diluted within a host material.

It is known in other contexts, that crystals can be induced to adopt polymorphic forms by the inclusion of impurities or dopants.[61] We reasoned that co-crystallising $[Fe(bpp)_2][ClO_4]_2$ with another $[M(bpp)_2][ClO_4]_2$ compound might force the iron complex to crystallise in an SCO-active form, if the dopant M^{2+} is a less plastic metal ion which is more resistant to the angular distortion. That could be a useful route to new SCO materials, if the dopant concentration needed to induce SCO is sufficiently small to retain their cooperative switching properties.[38,62] This is a proof-of-principle study of this concept.
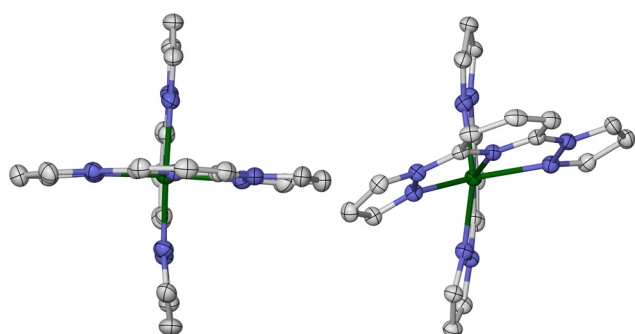

Fig. 1 Crystallographic high-spin molecular geometries in SCO-active $[Fe(bpp)_2][BF_4]_2$ ($P2_1$ phase, left),[26] and $[Fe(bpp)_2][ClO_4]_2$ (C2/c phase, right) which does not exhibit SCO.[35] H atoms are omitted for clarity. Colour code: C, white; N, blue; Fe, green.

Results and discussion

Selection of a suitable dopant molecule

To identify a suitable dopant species, a gas phase DFT study was undertaken at the ω-B97X-D/6-311G** level (we used the same protocol in a recent survey of the structural preferences of the angular distortion).[28] Different $[M(bpp)_2]^{2+}$ complexes were minimised at stages along the angular distortion, by fixing the *trans*-N{pyridyl}-M-N{pyridyl} angle (ϕ) to values between $165 \leq \phi \leq 155°$;[26,63] the lower limit is the experimental value of ϕ in $[Fe(bpp)_2][ClO_4]_2$.[35] The metal ions listed below were examined because salts of those $[M(bpp)_2]^{2+}$ complexes are known to be isomorphous with one of the iron complex phases shown in Fig. 1.[42,47,54,57,64–67]

The energy penalty associated with the distortion, ΔE(dist), for the different complexes runs as follows (Fig. 2 and ESI;† HS = high-spin):

$$M^{2+} = Fe^{2+}(HS) \approx Mn^{2+}(HS) < Zn^{2+}$$
$$\approx Co^{2+}(HS) \sim Cu^{2+} \ll Ni^{2+} \ll Ru^{2+}$$

The ΔE(dist) values for $[Fe(bpp)_2]^{2+}$ by this protocol are <1 kcal mol^{-1},[28] which is consistent with previous studies of this type using different functionals.[26,27,68–70]

$[Ni(bpp)_2]^{2+}$ was chosen as the dopant for this study, for three reasons. It shows a higher ΔE(dist) distortion energy than the other potential dopants, except the ruthenium complex. It is more synthetically accessible than its ruthenium analogue. Lastly, doping iron(II) SCO materials with nickel(II) has little effect on their transition temperature ($T_{\frac{1}{2}}$), which simplifies the interpretation of these results.[40,42–44,48,52,55,71]

Crystalline $[Ni(bpp)_2][ClO_4]_2$ (monoclinic, space group $P2_1$, $Z = 2$) is not isomorphous with $[Fe(bpp)_2][ClO_4]_2$ (monoclinic, $C2/c$, $Z = 4$). However it is isomorphous with both

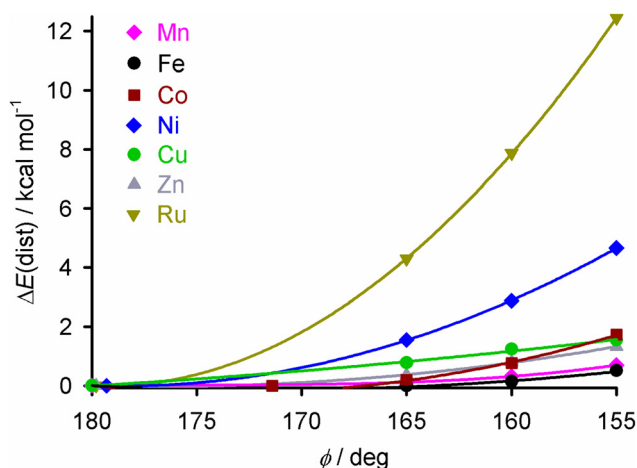**Fig. 2** The energy penalty associated with the angular distortion [ΔE(dist)] for different $[M(bpp)_2]^{2+}$ complexes. ΔE(dist) is the energy of each minimisation relative to the corresponding molecule with an undistorted structure; see the ESI† for more details. The data for the iron complex are taken from ref. 28.

[Ni(bpp)$_2$][BF$_4$]$_2$ [64] and the SCO-active salt [Fe(bpp)$_2$][BF$_4$]$_2$,[26] which adopt the same $P2_1$ phase. The cation in [Ni(bpp)$_2$][ClO$_4$]$_2$ exhibits an undistorted six-coordinate geometry, with no unusual features (Fig. S2†).

Composition and SCO properties of the solid solutions

Preformed [Fe(bpp)$_2$][ClO$_4$]$_2$ and [Ni(bpp)$_2$][ClO$_4$]$_2$ were co-crystallised from acetonitrile, using diethyl ether as antisolvent. Four compositions of the [Fe$_x$Ni$_{1-x}$(bpp)$_2$][ClO$_4$]$_2$ solid solutions were investigated in two solid forms; as polycrystalline materials grown over 1–2 days by a vapour diffusion method (**1a–4a**; Table 1), and as rapidly precipitated powders (**1b–4b**). The analytical compositions of the materials were confirmed by elemental microanalysis, EDX measurements and from their magnetic susceptibility data (Table 1). EDX element maps confirm the iron and nickel content is homogeneously distributed through each material (Fig. S1†).

The fractional metal compositions (x) deduced in this way were within experimental error of the synthetic stoichiometry used for all the doped materials. Different samples of slowly crystallised **1a–4a**, and rapidly precipitated **1b**, showed consistent structural and magnetic properties. However, the crystallinity (by powder diffraction) and magnetic behaviour showed some variability between different samples of **2b–4b**. Representative examples of each composition of **2b–4b** are described below.

X-ray powder diffraction show the polycrystalline materials adopt purely the $P2_1$ phase when x = 0.50 (**1a**, Table 1) and 0.73 (**2a**); and form a mixture of the $P2_1$ and $C2/c$ phases when x = 0.88 (**3a**) and 0.94 (**4a**; Fig. 3). That is, 26% nickel doping is sufficient to produce the pure $P2_1$ phase under these conditions. The high-spin $C2/c$ phase is the main component of **3a** and **4a**, but the presence of a $P2_1$ fraction is indicated by a low-angle shoulder at 2θ = 11.1°, for example, which becomes weaker as x approaches 1.

The powder patterns of **1b** and **4b** are essentially identical to their congeners **1a** and **4a** (Fig. 3). However, the diffraction peaks for **2b** and **3b** are broadened, implying those samples have reduced crystallinity. The powder patterns of **2b** and **3b** can both be simulated as mixed-phase materials, with **3b** having a lower fraction of the $P2_1$ phase.

All the powder patterns were reproduced by simulations using phase compositions deduced from the magnetic data, as described below (Fig. 3). A previous study of mixed-phase materials comprised of different iron complex salts, proposed that the $C2/c$ phase is the thermodynamic crystallisation product but the $P2_1$ phase is the kinetic product which is favoured by rapid precipitation.[72] That relationship is less clear in this mixed-metal system, however.

The iron content in all the compounds is high-spin at room temperature, with $\chi_M T$ at 300 K close to the expected values based on their metal composition (Table 1). **1a** and **2a** exhibit SCO centred at 250 ± 1 K, which is respectively gradual (**1a**), and abrupt with a small thermal hysteresis (**2a**; Fig. 4). The completeness of the transition (y, Table 1) is >98% based on their measured iron content. SCO in **3a** and **4a** resembles **2a** but only occurs in *ca.* 32% (**3a**) or 6% (**4a**) of the iron content in the samples, with the rest of their iron remaining high-spin on further cooling.

These data are consistent with the phase composition of the samples predicted by powder diffraction. Both **1a** and **2a** adopt the SCO-active $P2_1$ phase, while **3a** and **4a** are mixed-phase materials. Assuming that the $P2_1$ phase contains the nickel $(1 - x)$ plus the SCO-active fraction (y) of the iron content in the sample (x), the fraction of the material adopting the $P2_1$ phase ($\omega\{P2_1\}$) can be estimated by eqn (1):

$$\omega\{P2_1\} = xy + (1 - x) \tag{1}$$

This predicts $P2_1 : C2/c$ phase ratios of 0.40 : 0.60 for **3a** and 0.12 : 0.88 for **4a** (Table 1); simulated powder patterns based

Table 1 Compositions and spin-crossover parameters for the [Fe$_x$Ni$_{1-x}$(bpp)$_2$][ClO$_4$]$_2$ solid solutions, from magnetic susceptibility data. Estimated errors are ±0.03 on x and y, ±0.05 on $\omega\{P2_1\}$ and up to ±0.1 on z [a]

	x	y	$\omega\{P2_1\}$	z	$T_{\frac{1}{2}}\downarrow$/K	$T_{\frac{1}{2}}\uparrow$/K	$\chi_M T/\text{cm}^3\ \text{mol}^{-1}\ \text{K}$ $T = 300$ K	HS$_{\text{calc}}$[b]	$T = 100$ K	LS$_{\text{calc}}$[b]
Polycrystalline										
1a	0.53	0.97	0.98	0.52	249	249	2.35	2.42	0.62	0.56
2a	0.74	0.98	0.98	0.74	249	251	2.87	2.90	0.37	0.31
3a	0.87	0.32[c]	0.40[c]	0.68[c]	250	251	3.21	3.20	2.19 [2.24[d]]	0.16
4a	0.94	0.06[c]	0.12[c]	0.50[c]	250	251	3.38	3.36	3.13 [3.15[d]]	0.07
Powder										
1b	0.52	0.97	0.98	0.51	246	246	2.29	2.39	0.63	0.58
2b	0.74	0.64[c]	0.73[c]	0.64[c]	248	249	2.81	2.90	0.90 [1.25[d]]	0.31
3b	0.88	0.55[c]	0.61[c]	0.80[c]	248	250	3.16	3.22	1.33 [1.52[d]]	0.14
4b	0.93	0.07[c]	0.14[c]	0.48[c]	248	248	3.33	3.34	2.97 [3.11[d]]	0.08

[a] y is the completeness of the spin-transition in the magnetic measurements; $\omega\{P2_1\}$ is the fraction of the sample adopting the $P2_1$ phase [eqn (1)]; and z gives the metal composition of the $P2_1$ fraction of the sample [eqn (2)]. [b] Calculated from x, using these values for the constituent compounds: [Ni(bpp)$_2$][BF$_4$]$_2$, 1.2 cm^3 mol^{-1} K; high-spin [Fe(bpp)$_2$][BF$_4$]$_2$, 3.5 cm^3 mol^{-1} K; low-spin [Fe(bpp)$_2$][BF$_4$]$_2$, 0.[42] [c] Calculated from $\chi_M T$ at 230 K to exclude SCO in any amorphous fraction of the sample at lower temperatures. [d] This is $\chi_M T$ at 230 K, just below the abrupt partial spin-transition, which is given for the mixed phase samples in the Table. **2b–4b** show an additional slow monotonic decrease in $\chi_M T$ on further cooling, which implies a fraction of the material is amorphous (Fig. S6†).
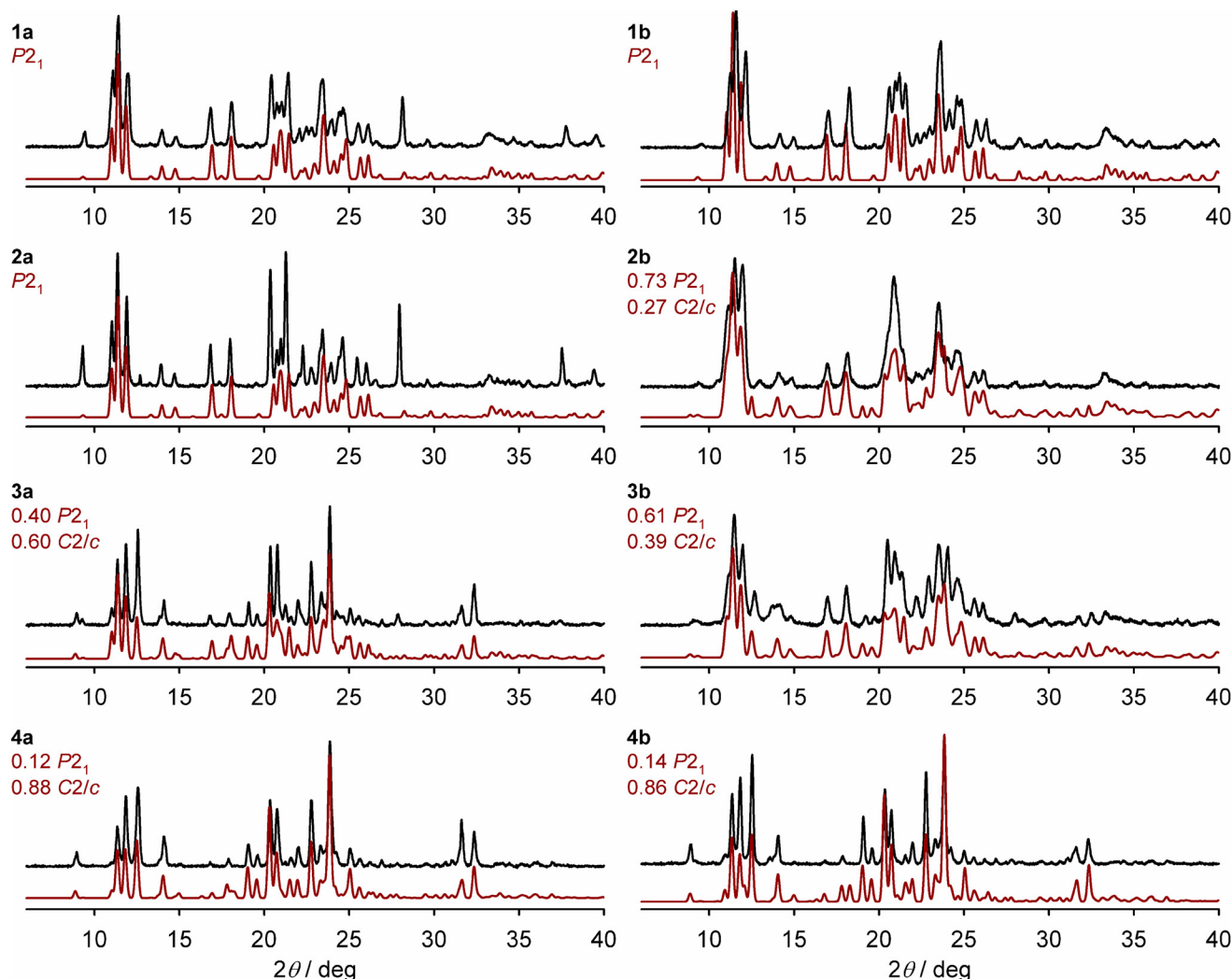
Fig. 3 Room temperature X-ray powder patterns for the solid solutions (black), and simulations derived from the single crystal X-ray structures of the precursor materials (red; details in the Experimental section). The composition of phases employed in each simulation is derived from the $\omega\{P2_1\}$ values in Table 1, although that doesn't account for the presence of amorphous material evident in the magnetic data for **2b–4b** (Fig. S6†). Differences in peak intensities between the measured and simulated data arise from preferred orientation effects, which are more pronounced for polycrystalline **1a–4a**.

on those compositions are excellent matches for the data (Fig. 3). The metal content of that $P2_1$ fraction is then $[Fe_zNi_{1-z}]$ (eqn (2)):

$$z = \frac{xy}{\omega\{P2_1\}} \quad (2)$$

This gives $z = 0.68$ for **3a** and 0.50 for **4a**, which are lower than the iron content of the samples as a whole (Table 1). That is, the SCO-active $P2_1$ fractions of **3a** and **4a** are enriched in nickel. In contrast, z for **1a** and **2a** is equal to their stoichiometric composition x, within experimental error.

The thermal SCO equilibrium in **1b** occurs a little more gradually than for **1a**, and is centred at slightly lower temperature (Fig. S6†). In other respects, the properties of those two materials are identical within experimental error. However, magnetic data for **2b–4b** show more differences from their

slowly crystallised counterparts. Each sample undergoes abrupt partial SCO just below 250 K, which is then followed by a very gradual, almost monotonic decrease in $\chi_M T$ on further cooling (Fig. S6†). The latter feature is characteristic of amorphous solids containing SCO centres, where they are less densely packed in heterogeneous chemical environments.[38,73,74] The abrupt spin-transitions in **2b** and **3b** each proceed to *ca.* 50% completeness based on their iron content, but with **2b** exhibiting a more pronounced amorphous tail at lower temperatures. The data imply $\omega\{P2_1\}$ follows a consistent trend in the rapidly precipitate samples (Table 1):

1b ($\omega\{P2_1\} = 0.98$) > **2b** (0.67) > **3b** (0.56) > **4b** (0.13)

The remainder of each of these samples is a mixture of the $C2/c$ phase and a smaller quantity of amorphous material. The SCO-active $P2_1$ phase is calculated to be more iron-rich in **3b** (z
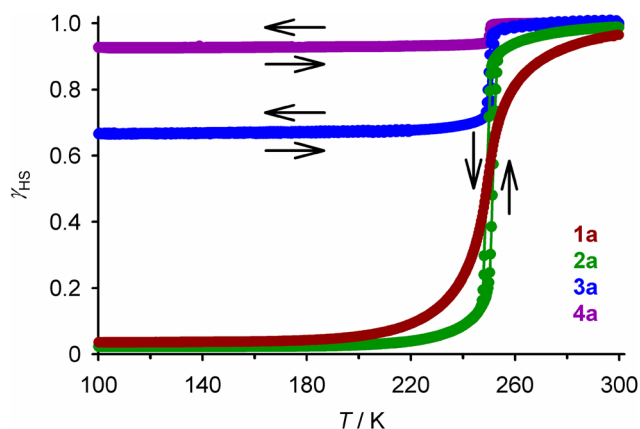
Fig. 4 The spin-transitions shown by polycrystalline **1a**–**4a**, from magnetic susceptibility data measured in cooling and warming modes at a scan rate of 2 K min^{-1}. The graph shows the high-spin fraction of the iron content in the sample (γ_{HS}) at each temperature, with data for each compound connected by a spline curve for clarity. $\chi_M T$ vs. T plots for all the samples in Table 1 are given in Fig. S6.†

= 0.80) than in **2b** (z = 0.64) or **3a** (z = 0.68). However the error on that calculation should increase as $\omega\{P2_1\}$ decreases, and could be as high as ±0.1 for **3a**/**3b**.

The midpoint temperature ($T_{\frac{1}{2}}$) for the spin transitions in all these samples is very similar, at 246 ≤ $T_{\frac{1}{2}}$ ≤ 251 K (Table 1). That small variation is consistent with other iron(II) compounds containing isomorphous nickel(II) dopants,[40,42–44,48,52,55,71] including [Fe$_x$Ni$_{1-x}$(bpp)$_2$][BF$_4$]$_2$.[42] The SCO cooperativity shown by **1a**/**1b** and **3a**/**3b** closely resembles that in [Fe$_x$Ni$_{1-x}$(bpp)$_2$][BF$_4$]$_2$ materials with comparable compositions. However, the spin transition in **2a** is more abrupt than its closest analogue from the BF$_4^-$ series (Fig. S7†).

The SCO-active perchlorates in this work exhibit $T_{\frac{1}{2}}$ 10 ± 1 K below the corresponding BF$_4^-$ salt materials.[42] That should reflect the larger volume of the perchlorate anion,[75] which leads to an expansion of the ClO$_4^-$-containing $P2_1$ lattice. That expansion additionally stabilises the high-spin state of the iron complex, whose molecular volume is 1.4% larger than the low-spin form,[76] thus lowering $T_{\frac{1}{2}}$. While counter examples exist,[77–80] an inverse relationship between $T_{\frac{1}{2}}$ and anion size is most commonly found when isomorphous salts of the same complex with weakly interacting anions are compared.[77,80–88]

Crystallographic characterisation

Single crystals of **1a** and **2a** (both monoclinic, $P2_1$, Z = 2) are isomorphous with [Ni(bpp)$_2$][ClO$_4$]$_2$. Full structure refinements of **1a** were achieved in its high- and low-spin states, at 300 and 100 K respectively (Fig. S8†). However crystals of **2a** diffracted poorly above *ca.* 200 K, and did not afford a satisfactory high-spin dataset. That could be a consequence of their containing almost the maximum iron content consistent with the $P2_1$ phase. Better data were obtained at lower temperatures, and a precise structure refinement of low-spin **2a** was also achieved at 100 K (Fig. S9†). The metal content x of the crystals at 100 K refined as 0.50(2) for **1a** and 0.76(3) for **2a**.

The structure refinements contain a crystallographically ordered [Fe$_x$Ni$_{1-x}$(bpp)$_2$]$^{2+}$ molecule, with partial iron and nickel atoms having the same atomic coordinates and displacement parameters. That is the approach taken in other crystallographic studies of doped SCO crystals.[55,89–92] Metric parameters from the refinements are consistent with statistical mixtures of the low-spin iron(II) and nickel(II) complexes, in those ratios (Table S6†).[54] That is useful confirmation of the crystal metal stoichiometries in the previous paragraph.

Attempts to resolve the fractional [Fe(bpp)$_2$]$^{2+}$ and [Ni(bpp)$_2$]$^{2+}$ molecules in **1a** and **2a** at 100 K required numerous distance and thermal parameter restraints, which made them less useful as probes of molecular structure. Such disorder models were achieved in [Fe$_x$M$_{1-x}$(bpp)$_2$][BF$_4$]$_2$ cocrystals using higher resolution datasets collected with synchrotron radiation.[54] Synchrotron data were not obtained for **1a** and **2a** in this work, however.

Variable temperature unit cell measurements demonstrate gradual thermal SCO in the crystal of **1a** with $T_{\frac{1}{2}}$ = 245 ± 3 K; and, an abrupt spin-transition for the crystal of **2a** at $T_{\frac{1}{2}}$ = 255 ± 5 K (Fig. 5 and S13, S14†). These behaviours are broadly consistent with the magnetic data for both compounds (Fig. 5 and S6†). The changes to the unit cell dimensions during SCO resemble our previous study of the [Fe$_x$Ni$_{1-x}$(bpp)$_2$][BF$_4$]$_2$ system (Table S9†).[54] The isothermal volume change during high → low-spin SCO at $T_{\frac{1}{2}}$ (ΔV_{SCO}) for **1a** [−19.0(5) Å^3] is identical to that of a [Fe$_x$Ni$_{1-x}$(bpp)$_2$][BF$_4$]$_2$ crystal with a similar metal content [−18.8(3) Å^3],[54] within experimental error. However ΔV_{SCO} for **2a** [−21.9(6) Å^3] is *ca.* 3 Å^3 smaller than expected, based on data from the BF$_4^-$ salt materials (Fig. S14†).[93] Its a, b and c unit cell dimensions all undergo smaller changes during SCO than predicted from its composition (Table S9†). While its low-spin crystal structure is as-expected (Table S6†), a high-spin structure refinement of **2a** was not achieved. So, the structural basis for that anomaly is unclear. The small ΔV_{SCO} of **2a** has no impact on the abruptness of its spin-transition, however.[62]

The complex molecules in the $P2_1$ phase pack into 2D "terpyridine embrace" layers[94] in the (001) plane, through interdigitation of their pyrazolyl arms *via* face-to-face C–H···π and edge-to-face π···π contacts (Fig. S10 and S11†).[54] Neighbouring cation layers associate more loosely along c, and are separated by the ClO$_4^-$ ions. [Fe(bpp)$_2$]$^{2+}$ derivatives with this crystal packing motif often show abrupt thermal spin-transitions with narrow thermal hysteresis;[95,96] the magnetic data from **2a** and **3a** imply the $P2_1$ phase of [Fe(bpp)$_2$][ClO$_4$]$_2$ behaves similarly (Fig. 4).

Other salts of [Fe(bpp)$_2$]$^{2+}$ and [Ni(bpp)$_2$]$^{2+}$

Solid [Fe(bpp)$_2$][PF$_6$]$_2$ is high-spin, and crystallises in the $C2/c$ crystal phase.[26] A crystal structure of [Fe(bpp)$_2$][CF$_3$SO$_3$]$_2$ in the $C2/c$ phase is also available,[28] although bulk samples of that salt contain a mixture of phases by powder diffraction (Fig. S16†). Hence, [Ni(bpp)$_2$][PF$_6$]$_2$ and [Ni(bpp)$_2$][CF$_3$SO$_3$]$_2$ were also investigated as potential dopants in this study. However crystals of those compounds were difficult to obtain, and decom-
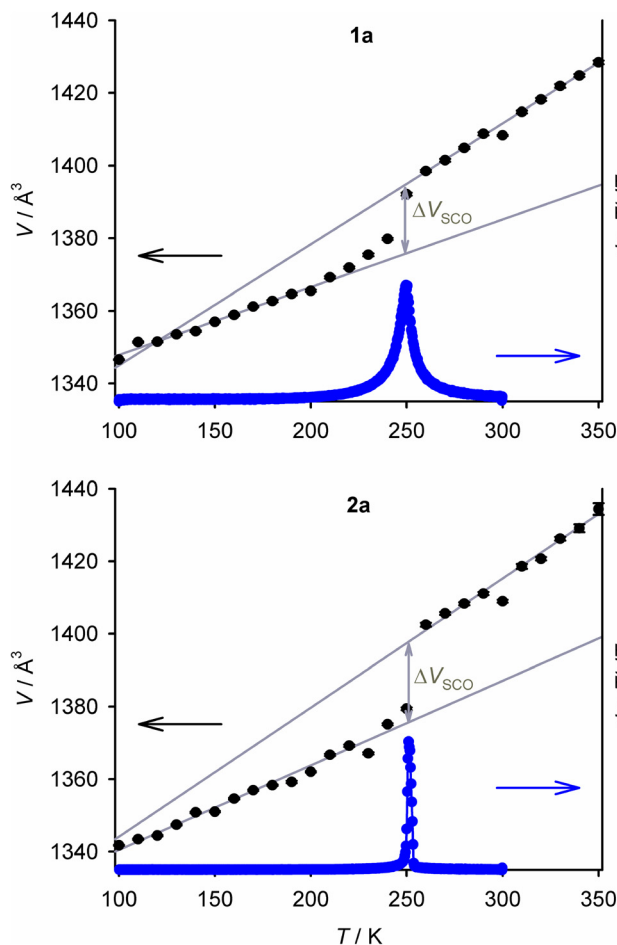
Fig. 5 Variable temperature unit cell volumes for **1a** (top) and **2a** (bottom). The grey lines show the thermal expansion linear regression fits for the volume change at $T_{\frac{1}{2}}$ (ΔV_{SCO}). The first derivative of the magnetic susceptibility data for each compound is also plotted to an arbitrary scale, as blue data points connected by a spline curve.

posed rapidly outside their mother liquor which prevented their structural characterisation. Powder samples of $[Ni(bpp)_2][PF_6]_2$ and $[Ni(bpp)_2][CF_3SO_3]_2$ are not isomorphous by X-ray powder diffraction, and neither salt adopts the $P2_1$ phase (Fig. S15 and S16†). Since structures of the nickel complex host lattices could not be determined, solid solutions of those iron and nickel complex salts were not pursued further.

Conclusions

High-spin $[Fe(bpp)_2][ClO_4]_2$, which adopts the $C2/c$ crystal phase, can be induced to crystallise in the SCO-active $P2_1$ phase by doping with $[Ni(bpp)_2][ClO_4]_2$. (Poly)crystalline solid solutions $[Fe_xNi_{1-x}(bpp)_2][ClO_4]_2$ with $x = 0.54$ (**1a**) or 0.74 (**2a**), produced under slow crystallisation conditions, are phase-pure and exhibit gradual (**1a**) or abrupt (**2a**) SCO at $T_{\frac{1}{2}} = 250 \pm 1$ K. Both transitions proceed to *ca.* 98% completeness based on their iron content (Fig. 4). Analogous materials with $x = 0.87$ (**3a**) and 0.94 (**4a**) have a mixed phase composition, with the

high-spin $C2/c$ phase as the major component. Those samples exhibit partial spin-transitions which resemble **2a**, but are incomplete.

Rapidly precipitated powders with the same compositions (**1b–4b**) behave similarly, except that **2b–4b** appear to contain an amorphous fraction as well as the two crystalline phases. Hence materials with the best-defined phase compositions and SCO properties are produced by slow crystallisation in this system. On the basis of Table 1, the maximum iron content that can be present in the $P2_1$ phase is estimated at $z = 0.7 \pm 0.1$ (eqn (2)). Surplus iron in the more iron-rich samples, which cannot be accommodated within their $P2_1$ crystallites, is then present as the $C2/c$ or (for **2b–4b**) amorphous material.

The dependence of $T_{\frac{1}{2}}$ on the composition of **1a–4a** resembles that found in isomorphous $[Fe_xNi_{1-x}(bpp)_2][BF_4]_2$ (Fig. S14†). The putative $P2_1$ phase of $[Fe(bpp)_2][ClO_4]_2$ itself is predicted to show $T_{\frac{1}{2}} = 251 \pm 1$ K, which is 10 K below that of isomorphous BF_4^- salt.[72] That is consistent with the behaviour of most other isomorphous salts of SCO compounds containing those anions.[77,80–88] Interestingly, the isothermal unit cell volume change during SCO (ΔV_{SCO}) for **1a** and **2a** does not mirror the trend shown by the $[Fe_xNi_{1-x}(bpp)_2][BF_4]_2$ series, with ΔV_{SCO} for **2a** being smaller than expected.[93] The poor X-ray diffraction exhibited by crystals of **2a** at room temperature also contrasts with **1a**, and other $[M(bpp)_2]^{2+}$ complex salts exhibiting the $P2_1$ phase.[26,54,64–66,72] These anomalies may reflect the metal stoichiometry of **2a** ($x = 0.74$), which is around the maximum iron content that the $P2_1$ phase can accommodate; that merits further investigation.

In conclusion, 26% nickel(II) doping is sufficient to convert high-spin $[Fe(bpp)_2][ClO_4]_2$ into a single phase (poly)crystalline material showing a complete, cooperative thermal spin-transition. These are rare examples of SCO solid solutions formed from non-isomorphous constituents.[42,57–59] This is also the first demonstration of a new method for producing SCO compounds from nominally inert precursors, which could further expand the range of available SCO materials.

Experimental

2,6-Bis(pyrazol-1-yl)pyridine (bpp),[97] $[Fe(bpp)_2][ClO_4]_2$,[35] $[Fe(bpp)_2][PF_6]_2$[26] and $[Fe(bpp)_2][CF_3SO_3]_2$[28] were prepared by the published procedures.

CAUTION We experienced no problems using the perchlorate salts in this study, but metal–organic perchlorates are potentially explosive and should be handled with care in small quantities.

Synthesis of $[Ni(bpp)_2][ClO_4]_2$

A mixture of $Ni[ClO_4]_2 \cdot 6H_2O$ (0.22 g, 0.59 mmol) and bpp (0.25 g, 1.2 mmol) in acetonitrile (25 cm³) was stirred at room temperature until all the solid had dissolved. The blue solution was concentrated to *ca.* 10 cm³, then filtered. Slow diffusion of diethyl ether vapour into the solution yielded large blue crystals of the product complex. Yield 0.31g, 77%.

Found C, 38.9; H, 2.53; N, 20.3%. Calcd for $C_{22}H_{18}Cl_2N_{10}NiO_8$ C, 38.9; H, 2.67; N, 20.6%.

Synthesis of $[Ni(bpp)_2][PF_6]_2$

A mixture of $NiCl_2 \cdot 6H_2O$ (0.14 g, 0.59 mmol), bpp (0.25 g, 1.2 mmol) and $AgPF_6$ (0.30 g, 1.2 mmol) in acetonitrile (25 cm^3) was stirred at room temperature for 1 h. The resultant mixture was allowed to settle, then filtered to remove the AgCl precipitate and concentrated to *ca.* 10 cm^3. Addition of excess diethyl ether to the filtrate yielded a blue powder, which was collected and dried *in vacuo*. Yield 0.33 g, 72%. Found C, 34.1; H, 1.91; N, 18.3%. Calcd for $C_{22}H_{18}F_{12}N_{10}NiP_2$ C, 34.3; H, 2.35; N, 18.2%.

Synthesis of $[Ni(bpp)_2][CF_3SO_3]_2$

Method as for $[Ni(bpp)_2][ClO_4]_2$, using $Ni[CF_3SO_3]_2$ (0.21 g, 0.59 mmol). The product was a blue powder. Yield 0.31 g, 68%. Found C, 36.9; H, 2.00; N, 18.0%. Calcd for $C_{24}H_{18}F_6N_{10}NiO_6S_2$ C, 37.0; H, 2.33; N, 18.0%.

While $[Ni(bpp)_2][PF_6]_2$ and $[Ni(bpp)_2][CF_3SO_3]_2$ are tractable as rapidly precipitated powders, attempted crystallisations of both salts gave similar results. Slow diffusion of diethyl ether vapour into solutions of the compounds in common organic solvents sometimes gave crystals with an ingrown plate morphology, if the dehydrating agent triethyl orthoformate was added to the solution. These crystals decomposed rapidly when removed from the original mother liquor, however. Other crystallisations under the same conditions instead afforded blue oils, while recrystallisations using di-iso-propylether or methyl(*tert*-butyl)ether as the antisolvent also led to oils. Hence, no crystal structure determination was achieved for these salts.

Synthesis of $[Fe_xNi_{1-x}(bpp)_2][ClO_4]_2$ (1–4)

Preformed $[Fe(bpp)_2][ClO_4]_2$ and $[Ni(bpp)_2][ClO_4]_2$ were mixed in different mole ratios, to a combined mass of 0.25 g. The combined solids were stirred in acetonitrile (25 cm^3), until all the solid had dissolved. The solutions were concentrated to *ca.* 10 cm^3, then filtered. Slow diffusion of diethyl ether vapour into the filtered solutions over a period of 48 h afforded the polycrystalline materials **1a–4a**. Alternatively the powder samples **1b–4b** were produced by rapid addition of excess diethyl ether to these same filtered solutions, yielding a fine precipitate which was stored at 255 K for 18 h, then collected and dried *in vacuo*. Crystallised yields were in the range 80–85%.

The materials with high iron content are yellow at room temperature, which progresses towards a green colour as the nickel concentration increases. The compositions and analytical data for the solid solutions are given in Table S1.†

Single crystal X-ray structures

Single crystals of the precursor complexes were obtained by slow diffusion of diethyl ether vapour into solutions of the compounds in nitromethane. Crystals of **1a** and **2a** were obtained similarly, from acetonitrile solution. Diffraction data were measured with an Agilent Supernova or a Nonius Kappa-CCD diffractometer, which were fitted with an Oxford Cryostream low-temperature device. Monochromated Cu-K$_\alpha$ (λ = 1.5418 Å) or Mo-K$_\alpha$ (λ = 0.7107 Å) radiation was used for different measurements.

Experimental details of the structure determinations are given in Table S2.† All the structures were solved by direct methods (SHELXTL[98]), and developed by full least-squares refinement on F^2 (SHELXL-2018 [99]). Crystallographic figures and powder pattern simulations were prepared using XSEED,[100] and other publication materials were prepared using Olex2.[101]

CCDC 2332656–2332661† contain the supplementary crystallographic data for this paper.

Other measurements

Elemental microanalyses were performed by the microanalytical service at the London Metropolitan University School of Human Sciences. SEM images and EDX measurements were obtained using an FEI Nova NanoSEM 450 environmental microscope, operating at 3 kV. Magnetic susceptibility measurements were performed on a Quantum Design MPMS-3 VSM magnetometer, with an applied field of 5000 G and a scan rate of 2 K min^{-1}. A diamagnetic correction for the sample was estimated from Pascal's constants;[102] a previously measured diamagnetic correction for the sample holder was also applied to the data.

X-ray powder diffraction patterns were measured at room temperature using a Bruker D2 phaser diffractometer. Simulations of the solid solution powder patterns in Fig. 3 were based on the structure refinement of $[Fe(bpp)_2][ClO_4]_2$ at 300 K in this work (*C*2/*c* phase); and, a model derived from the published structure of $[Fe(bpp)_2][BF_4]_2$ at 290 K,[26] with the BF_4^- ions replaced by ClO_4^- (*P*2$_1$ phase). Some minor differences between measured and simulated 2θ values in Fig. 3 reflect small discrepancies between the unit cell dimensions in that model and the hypothetical *P*2$_1$ phase of $[Fe(bpp)_2][ClO_4]_2$.

DFT minimizations of $[M(bpp)_2]^{2+}$ were performed using Spartan'20 [103] with the ω-B97X-D functional and 6-311G** basis set.[104] Molecules with $S = 0$ ($M^{2+} = Zn^{2+}$ and Ru^{2+}) were treated as spin-restricted, while molecules with $S \geq \frac{1}{2}$ ($M^{2+} = Mn^{2+}$, Co^{2+}, Ni^{2+} and Cu^{2+}) were treated as spin-unrestricted. The calculations were performed in the gas phase because solvent gradients for transition ions are not implemented in Spartan'20. Initial models were constructed *de novo* with ϕ restrained to the appropriate value, then subjected to a preliminary molecular mechanics minimization before the full DFT geometry minimization calculation. The computational results for $[Fe(bpp)_2]^{2+}$ are reproduced from ref. 28.

Data availability

Data supporting this study are available in the ESI,† or at **https://doi.org/10.5518/1493**.

Author contributions

Conflicts of interest

There are no conflicts to declare.

Acknowledgements

References

1 *Spin Crossover in Transition Metal Compounds I–III: Topics in Current Chemistry*, ed. P. Gütlich and H. A. Goodwin, Springer-Verlag, Berlin, 2004, vol. 233–235.

2 *Spin-crossover materials – properties and applications*, ed. M. A. Halcrow, John Wiley & Sons, Chichester, UK, 2013, p. 568.

3 J. Zarembowitch, F. Varret, A. Hauser, J. A. Real and K. Boukheddaden, *C. R. Chim.*, 2018, **21**, 1056–1059.

4 W. Huang, X. Ma, O. Sato and D. Wu, *Chem. Soc. Rev.*, 2021, **50**, 6832–6870.

5 M. K. Javed, A. Sulaiman, M. Yamashita and Z.-Y. Li, *Coord. Chem. Rev.*, 2022, **467**, 214625.

6 Y. Sekine, R. Akiyoshi and S. Hayami, *Coord. Chem. Rev.*, 2022, **469**, 214663.

7 E. Resines-Urien, E. Fernandez-Bartolome, A. Martinez-Martinez, A. Gamonal, L. Piñeiro-López and J. S. Costa, *Chem. Soc. Rev.*, 2023, **52**, 705–727.

8 M. D. Manrique-Juárez, S. Rat, L. Salmon, G. Molnár, C. M. Quintero, L. Nicu, H. J. Shepherd and A. Bousseksou, *Coord. Chem. Rev.*, 2016, **308**, 395–408.

9 S. Rat, M. Piedrahita-Bello, L. Salmon, G. Molnár, P. Demont and A. Bousseksou, *Adv. Mater.*, 2018, **30**, 1703862.

10 E. Coronado, *Nat. Rev. Mater.*, 2020, **5**, 87–104.

11 K. S. Kumar and M. Ruben, *Angew. Chem., Int. Ed.*, 2021, **60**, 7502–7521.

12 R. Torres-Cavanillas, M. Gavara-Edo and E. Coronado, *Adv. Mater.*, 2024, **36**, 2307718.

13 M. Chergui and E. Collet, *Chem. Rev.*, 2017, **117**, 11025–11065.

14 S. Pillet, *J. Appl. Phys.*, 2021, **129**, 181101.

15 M. A. Halcrow, *Coord. Chem. Rev.*, 2009, **253**, 2493–2514.

16 L. J. Kershaw Cook, R. Mohammed, G. Sherborne, T. D. Roberts, S. Alvarez and M. A. Halcrow, *Coord. Chem. Rev.*, 2015, **289–290**, 2–12.

17 M. Attwood and S. S. Turner, *Coord. Chem. Rev.*, 2017, **353**, 247–277.

18 L. J. Kershaw Cook, R. Kulmaczewski, R. Mohammed, S. Dudley, S. A. Barrett, M. A. Little, R. J. Deeth and M. A. Halcrow, *Angew. Chem., Int. Ed.*, 2016, **55**, 4327–4331.

19 M. A. Halcrow, I. Capel Berdiell, C. M. Pask and R. Kulmaczewski, *Inorg. Chem.*, 2019, **58**, 9811–9821.

20 B. Schäfer, T. Bauer, I. Faus, J. A. Wolny, F. Dahms, O. Fuhr, S. Lebedkin, H.-C. Wille, K. Schlage, K. Chevalier, F. Rupp, R. Diller, V. Schünemann, M. M. Kappes and M. Ruben, *Dalton Trans.*, 2017, **46**, 2289–2302.

21 E. Burzurí, A. García-Fuente, V. García-Suárez, K. Senthil Kumar, M. Ruben, J. Ferrer and H. S. J. van der Zant, *Nanoscale*, 2018, **10**, 7905–7911.

22 F. Moreau, J. Marrot, F. Banse, C. Serre and A. Tissot, *J. Mater. Chem. C*, 2020, **8**, 16826–16833.

23 M. Palacios-Corella, J. Ramos-Soriano, M. Souto, D. Ananias, J. Calbo, E. Ortí, B. M. Illescas, M. Clemente-León, N. Martín and E. Coronado, *Chem. Sci.*, 2021, **12**, 757–766.

24 S.-Q. Su, S.-Q. Wu, Y.-B. Huang, W.-H. Xu, K.-G. Gao, A. Okazawa, H. Okajima, A. Sakamoto, S. Kanegawa and O. Sato, *Angew. Chem., Int. Ed.*, 2022, **61**, e202208771.

25 M. Palacios-Corella, V. García-López, J. C. Waerenborgh, B. J. C. Vieira, G. M. Espallargas, M. Clemente-León and E. Coronado, *Chem. Sci.*, 2023, **14**, 3048–3055.

26 J. M. Holland, J. A. McAllister, C. A. Kilner, M. Thornton-Pett, A. J. Bridgeman and M. A. Halcrow, *J. Chem. Soc., Dalton Trans.*, 2002, 548–554.

27 S. Vela, J. J. Novoa and J. Ribas-Arino, *Phys. Chem. Chem. Phys.*, 2014, **16**, 27012–27024.

28 I. Capel Berdiell, E. Michaels, O. Q. Munro and M. A. Halcrow, *Inorg. Chem.*, 2024, **63**, 2732–2744.

29 There are examples of $[Fe(bpp)_2]^{2+}$ derivatives that crystallise in distorted and undistorted polymorphs (ref. 105), or where distorted high-spin and undistorted SCO-active molecules co-crystallise in the same lattice (ref. 36, 106 and 107).

30 M. Matsuda, H. Isozaki and H. Tajima, *Chem. Lett.*, 2008, **37**, 374–375.

31 S. P. Vallone, A. N. Tantillo, A. M. dos Santos, J. Molaison, R. Kulmaczewski, A. Chapoy, P. Ahmadi, M. A. Halcrow and K. G. Sandeman, *Adv. Mater.*, 2019, **31**, 1807334.

32 M. Owczarek, M. Lee, S. Liu, E. R. Blake, C. S. Taylor, G. A. Newman, J. C. Eckert, J. H. Leal, T. A. Semelsberger, H.-P. Cheng, W. Nie and V. S. Zapf, *Angew. Chem., Int. Ed.*, 2022, **61**, e202214335.

33 N. Suaud, M.-L. Bonnet, C. Boilleau, P. Labèguerie and N. Guihéry, *J. Am. Chem. Soc.*, 2009, **131**, 715–722.

34 S. Vela, M. Fumanal and C. Sousa, *J. Mater. Chem. C*, 2023, **11**, 235–243.

35 J. Elhaïk, D. J. Evans, C. A. Kilner and M. A. Halcrow, *Dalton Trans.*, 2005, 1693–1700.

36 J. Elhaïk, C. A. Kilner and M. A. Halcrow, *Dalton Trans.*, 2006, 823–830.

37 Salts of $[Fe(bpp)_2]^{2+}$ with larger metallate or radical anions have also been reported, which show different spin state behaviours (ref. 36 and 108–110).

38 P. Gütlich, A. Hauser and H. Spiering, *Angew. Chem., Int. Ed. Engl.*, 1994, **33**, 2024–2054.

39 A. Hauser, J. Jeftić, H. Romstedt, R. Hinek and H. Spiering, *Coord. Chem. Rev.*, 1999, **190–192**, 471–491.

40 T. Tayagaki, A. Galet, G. Molnár, M. C. Muñoz, A. Zwick, K. Tanaka, J. A. Real and A. Bousseksou, *J. Phys. Chem. B*, 2005, **109**, 14859–14867.

41 C. Baldé, C. Desplanches, A. Wattiaux, P. Guionneau, P. Gütlich and J.-F. Létard, *Dalton Trans.*, 2008, 2702–2707.

42 C. A. Tovee, C. A. Kilner, J. A. Thomas and M. A. Halcrow, *CrystEngComm*, 2009, **11**, 2069–2077.

43 Z. Yu, T. Kuroda-Sowa, H. Kume, T. Okubo, M. Maekawa and M. Munakata, *Bull. Chem. Soc. Jpn.*, 2009, **82**, 333–337.

44 A. Rotaru, M. M. Dîrtu, C. Enachescu, R. Tanasa, J. Linares, A. Stancu and Y. Garcia, *Polyhedron*, 2009, **28**, 2531–2536.

45 N. Paradis, G. Chastanet, F. Varret and J.-F. Létard, *Eur. J. Inorg. Chem.*, 2013, 968–974.

46 N. Paradis, G. Chastanet, T. Palamarciuc, P. Rosa, F. Varret, K. Boukheddaden and J.-F. Létard, *J. Phys. Chem. C*, 2015, **119**, 20039–20050.

47 M. A. Halcrow and G. Chastanet, *Polyhedron*, 2017, **136**, 5–12.

48 B. R. Mullaney, L. Goux-Capes, D. J. Price, G. Chastanet, J.-F. Létard and C. J. Kepert, *Nat. Commun.*, 2017, **8**, 1053.

49 M. S. Sylla, C. Baldé, N. Daro, C. Desplanches, M. Marchivie and G. Chastanet, *Eur. J. Inorg. Chem.*, 2018, 297–304.

50 R. Diego, O. Roubeau and G. Aromí, *Chem. Sq.*, 2021, **5**, 1.

51 P. Chakraborty, M. Sy, H. Fourati, T. Delgado, M. Dutta, C. Das, C. Besnard, A. Hauser, C. Enachescu and K. Boukheddaden, *Phys. Chem. Chem. Phys.*, 2022, **24**, 982–994.

52 C. Das, S. Dey, A. Adak, C. Enachescu and P. Chakraborty, *Cryst. Growth Des.*, 2023, **23**, 3496–3508.

53 M. Dutta, S. Bisht, P. Ghosh, A. I. Chilug, D. Mann, C. Enachescu, M. Shatruk and P. Chakraborty, *Inorg. Chem.*, 2023, **62**, 15050–15062.

54 P. Ghosh, C. M. Pask, H. B. Vasili, N. Yoshinari, T. Konno, O. Cespedes, C. Enachescu, P. Chakraborty and M. A. Halcrow, *J. Mater. Chem. C*, 2023, **11**, 12570–12582.

55 X. Li, D. Zhang, Y. Qian, W. Liu, C. Mathonière, R. Clérac and X. Bao, *J. Am. Chem. Soc.*, 2023, **145**, 9564–9570.

56 F. Renz, H. Oshio, V. Ksenofontov, M. Waldeck, H. Spiering and P. Gütlich, *Angew. Chem., Int. Ed.*, 2000, **39**, 3699–3700.

57 M. A. Halcrow, *Chem. Commun.*, 2010, **46**, 4761–4763.

58 S. V. Tumanov, S. L. Veber, S. Greatorex, M. A. Halcrow and M. V. Fedin, *Inorg. Chem.*, 2018, **57**, 8709–8713.

59 C. Bartual-Murgui, C. Pérez-Padilla, S. J. Teat, O. Roubeau and G. Aromí, *Inorg. Chem.*, 2020, **59**, 12132–12142.

60 Y.-Y. Wu, Z.-Y. Li, S. Peng, Z.-Y. Zhang, H.-M. Cheng, H. Su, W.-Q. Hou, F.-L. Yang, S.-Q. Wu, O. Sato, J.-W. Dai, W. Li and X.-H. Bu, *J. Am. Chem. Soc.*, 2024, **146**, 8206–8215.

61 W. Kras, A. Carletta, R. Montis, R. A. Sullivan and A. J. Cruz-Cabeza, *Commun. Chem.*, 2021, **4**, 38.

62 A.-I. Popa, L. Stoleriu and C. Enachescu, *J. Appl. Phys.*, 2021, **129**, 131101.

63 While undistorted complexes show $\phi = 180°$, geometries with $180 \leq \phi \leq 143°$ have been observed experimentally in high-spin $[Fe(bpp)_2]^{2+}$ derivatives (ref. 16 and 28).

64 J. M. Holland, C. A. Kilner, M. Thornton-Pett and M. A. Halcrow, *Polyhedron*, 2001, **20**, 2829–2840.

65 M. A. Leech, N. K. Solanki, M. A. Halcrow, J. A. K. Howard and S. Dahaoui, *Chem. Commun.*, 1999, 2245–2246.

66 N. K. Solanki, M. A. Leech, E. J. L. McInnes, F. E. Mabbs, J. A. K. Howard, C. A. Kilner, J. M. Rawson and M. A. Halcrow, *J. Chem. Soc., Dalton Trans.*, 2002, 1295–1301.

67 K. N. Lazarou, I. Stamatopoulos, V. Psycharis, C. Duboc, C. P. Raptopoulou and Y. Sanakis, *Polyhedron*, 2018, **155**, 291–301.

68 I. Capel Berdiell, R. Kulmaczewski and M. A. Halcrow, *Inorg. Chem.*, 2017, **56**, 8817–8828.

69 J. Nance, D. N. Bowman, S. Mukherjee, C. T. Kelley and E. Jakubikova, *Inorg. Chem.*, 2015, **54**, 11259–11268.

70 H.-Y. Kwon, D. C. Ashley and E. Jakubikova, *Dalton Trans.*, 2021, **50**, 14566–14575.

71 J.-P. Martin, J. Zarembowitch, A. Dworkin, J. G. Haasnoot and E. Codjovi, *Inorg. Chem.*, 1994, **33**, 2617–2623.

72 C. Carbonera, C. A. Kilner, J.-F. Létard and M. A. Halcrow, *Dalton Trans.*, 2007, 1284–1292. This is a study of mixed-anion salts $[Fe(bpp)_2][BF_4]_x[ClO_4]_{2-x}$, $(0 < x < 2)$ which also adopt the $P2_1$ phase, the $C2/c$ phase or a mixture of both depending on their composition and the crystallisation conditions.

73 S. Bonnet, G. Molnár, J. S. Costa, M. A. Siegler, A. L. Spek, A. Bousseksou, W.-T. Fu, P. Gamez and J. Reedijk, *Chem. Mater.*, 2009, **21**, 1123–1136.

74 P. Chakraborty, M.-L. Boillot, A. Tissot and A. Hauser, *Angew. Chem., Int. Ed.*, 2013, **52**, 7139–7142.

75 D. M. P. Mingos and A. L. Rohl, *J. Chem. Soc., Dalton Trans.*, 1991, 3419–3425.

76 The volume of the complex molecule in $[Fe(bpp)_2][BF_4]_2$ (ref. 26), which exhibits the $P2_1$ lattice, is 349.9(5) Å^3 in the high-spin state at 290 K; and 343.3(5) Å^3 in the low-spin state at 240 K. These volumes were calculated with Olex2 (ref. 97).

77 M. A. Halcrow, *Chem. Soc. Rev.*, 2011, **40**, 4119–4142.

78 S. Heider, H. Petzold, G. Chastanet, S. Schlamp, T. Rüffer, B. Weber and J.-F. Létard, *Dalton Trans.*, 2013, **42**, 8575–8584.

79 V. García-López, M. Palacios-Corella, A. Abhervé, I. Pellicer-Carreño, C. Desplanches, M. Clemente-León and E. Coronado, *Dalton Trans.*, 2018, **47**, 16958–16968.

80 O. Roubeau, *Chem. – Eur. J.*, 2012, **18**, 15230–15244.

81 M. Tafili-Kryeziu, M. Weil, T. Muranaka, A. Bousseksou, M. Hasegawa, A. Jun and W. Linert, *Dalton Trans.*, 2013, **42**, 15796–15804.

82 R. Mohammed, G. Chastanet, F. Tuna, T. L. Malkin, S. A. Barrett, C. A. Kilner, J.-F. Létard and M. A. Halcrow, *Eur. J. Inorg. Chem.*, 2013, 819–831.

83 H. Phan, S. M. Benjamin, E. Steven, J. S. Brooks and M. Shatruk, *Angew. Chem., Int. Ed.*, 2015, **54**, 823–827.

84 Y.-Y. Zhu, H.-Q. Li, Z.-Y. Ding, X.-J. Lü, L. Zhao, Y.-S. Meng, T. Liu and S. Gao, *Inorg. Chem. Front.*, 2016, **3**, 1624–1636.

85 R. Kulmaczewski, E. Trzop, L. J. Kershaw Cook, E. Collet, G. Chastanet and M. A. Halcrow, *Chem. Commun.*, 2017, **53**, 13268–13271.

86 R. Díaz-Torres, W. Phonsri, K. S. Murray, L. Liu, M. Ahmed, S. M. Neville, P. Harding and D. J. Harding, *Inorg. Chem.*, 2020, **59**, 13784–13791.

87 I. Capel Berdiell, R. Kulmaczewski, N. Shahid, O. Cespedes and M. A. Halcrow, *Chem. Commun.*, 2021, **57**, 6566–6569.

88 N. Suryadevara, A. Mizuno, L. Spieker, S. Salamon, S. Sleziona, A. Maas, E. Pollmann, B. Heinrich, M. Schleberger, H. Wende, S. K. Kuppusamy and M. Ruben, *Chem. – Eur. J.*, 2022, **28**, e202103853.

89 J. Kusz, H. Spiering and P. Gütlich, *J. Appl. Crystallogr.*, 2004, **37**, 589–595.

90 C. Baldé, C. Desplanches, F. Le Gac, P. Guionneau and J.-F. Létard, *Dalton Trans.*, 2014, **43**, 7820–7829.

91 H. Wang, C. Baldé, A. Grosjean, C. Desplanches, P. Guionneau and G. Chastanet, *Dalton Trans.*, 2018, **47**, 14741–14750.

92 R. Diego, O. Roubeau and G. Aromí, *Chem. Sq.*, 2021, **5**, 1.

93 ΔV_{SCO} in SCO materials containing isomorphous dopants has been proposed to show a linear dependence with the dopant concentration (ref. 89). Since $[\text{Fe(bpp)}_2][\text{BF}_4]_2$ exhi-bits $\Delta V_{\text{SCO}} = -30.4(3)$ Å^3 (ref. 54), by extrapolation from **1a** ΔV_{SCO} for **2a** would be expected to be *ca.*, -25 Å^3 (Fig. S14†).

94 I. Dance and M. Scudder, *CrystEngComm*, 2009, **11**, 2233–2247.

95 R. Pritchard, C. A. Kilner and M. A. Halcrow, *Chem. Commun.*, 2007, 577–579.

96 E. Michaels, C. M. Pask, I. Capel Berdiell, H. B. Vasili, M. J. Howard, O. Cespedes and M. A. Halcrow, *Cryst. Growth Des.*, 2022, **22**, 6809–6817.

97 D. L. Jameson and K. A. Goldsby, *J. Org. Chem.*, 1990, **55**, 4992–4994.

98 G. M. Sheldrick, *Acta Crystallogr., Sect. A: Found. Adv.*, 2015, **71**, 3–8.

99 G. M. Sheldrick, *Acta Crystallogr., Sect. C: Struct. Chem.*, 2015, **71**, 3–8.

100 L. J. Barbour, *J. Appl. Crystallogr.*, 2020, **53**, 1141–1146.

101 O. V. Dolomanov, L. J. Bourhis, R. J. Gildea, J. A. K. Howard and H. Puschmann, *J. Appl. Crystallogr.*, 2009, **42**, 339–341.

102 C. J. O'Connor, *Prog. Inorg. Chem.*, 1982, **29**, 203–283.

103 *Spartan'20*, Wavefunction Inc., Irvine, CA, 2020.

104 J.-D. Chai and M. Head-Gordon, *Phys. Chem. Chem. Phys.*, 2008, **10**, 6615–6620.

105 M. Haryono, F. W. Heinemann, K. Petukhov, K. Gieb, P. Müller and A. Grohmann, *Eur. J. Inorg. Chem.*, 2009, 2136–2143.

106 R. Kulmaczewski, F. Bamiduro, O. Cespedes and M. A. Halcrow, *Chem. – Eur. J.*, 2021, **27**, 2082–2092.

107 K. H. Sugiyarto, D. Onggo, H. Akutsu, V. R. Reddy, H. Sutrisno, Y. Nakazawa and A. Bhattacharjee, *CrystEngComm*, 2021, **23**, 2854–2861.

108 M. Nihei, H. Tahira, N. Takahashi, Y. Otake, Y. Yamamura, K. Saito and H. Oshio, *J. Am. Chem. Soc.*, 2010, **132**, 3553–3560.

109 Ö. Üngor, E. S. Choi and M. Shatruk, *Eur. J. Inorg. Chem.*, 2021, 4812–4820.

110 J. Li, X.-P. Sun, S. Bi, M. Xu, S. Jia, Z. Tang, P. Ma, J. Wang, J. Tao and J. Niu, *Inorg. Chem.*, 2022, **61**, 17932–17936.